High Gain and Low-Driving-Voltage Photodetectors Enabled by Organolead Triiodide Perovskites

Rui Dong[1], Yanjun Fang[1], Jungseok Chae[2,3], Jun Dai,[4] Zhengguo Xiao[1], Qingfeng Dong[1], Yongbo Yuan[1], Andrea Centrone[2], Xiao Cheng Zeng[4,1] and Jinsong Huang[1*]

[1]Department of Mechanical and Materials Engineering, University of Nebraska-Lincoln, Lincoln, Nebraska 68588, USA.

[2]Center for Nanoscale Science and Technology, National Institute of Standards and Technology 100 Bureau Drive, Gaithersburg, MD 20899, USA.

[3]Maryland Nanocenter, University of Maryland, College Park, MD 20742 USA.

[4]Department of Chemistry, University of Nebraska-Lincoln, Lincoln, Nebraska 68588, USA.

Weak light sensing in the ultraviolet (UV), visible and near infrared (NIR) have broad applications in fields concerning both industry, defense and scientific research[1, 2]. Solution-processable optoelectronic materials, such as organic materials, nanomaterials or nanocomposites, have shown promise as active layers in large area, low-cost photodetectors, because they frequently provide photoconductive gain (defined as the number of charges flowing through an external circuit per incident photon). However, further improvement of their detection performance is hindered by their poor charge carrier mobilities[3, 4]. Organometal trihalide

---

[1]*E-mail: jhuang2@unl.edu, RD and YF contributed to this work equally.

perovskites (OTPs, with molecular structure of $CH_3NH_3PbX_3$, X=Cl, Br, I or mixed halide), is a new family of optoelectronic materials which combine solution processability with Hall mobilities comparable to that of crystalline silicon, potentially providing a paradigm shift for engineering of low cost, yet high performance photodetectors. In contrast to silicon, solution processed OTPs are direct bandgap semiconductors with a very large absorption coefficient reaching $\approx 10^5 \, cm^{-1}$ in the UV-Vis range [5]. OTP solar cells show promise for competing with commercial silicon solar cells because they had achieved remarkably high power conversion efficiency of $\approx$ 15 % to 18 % within only four years of development[5, 6, 7, 8]. More and more experimental evidences suggest that defects/traps may be abundant in the OTP layer, either within the bulk or at the surface[7-11]. Although these trap states are deleterious to photovoltaic devices, here we show that it is possible to exploit them to boost the performance of perovskites photodetectors with an ingenious device design.

In this manuscript, we fabricate and characterize solution-processed $CH_3NH_3PbI_3$ photodetectors combining a high photoconductive gain with a broad spectral response, ranging from the UV to the NIR. Benefitting from the trapped-hole-induced electron injection, the $CH_3NH_3PbI_3$ photodetector works as a photodiode in the dark and shows large photoconductive gain under illumination. The maximum device gain reached 489 ± 6 at a very low driving voltage of -1 V.

The devices studied here have a layered inverted structure (**Figure 1a**) where indium tin oxide (ITO) is the cathode, $CH_3NH_3PbI_3$ is the active layer, 4,4′-bis[(p-trichlorosilylpropylphenyl)phenylamino]-biphenyl (TPD-Si$_2$) serves the function of hole transporting/electron blocking layer, molybdenum trioxide (MoO_3) is used for anode work function modification, and silver (Ag) as the anode. The $CH_3NH_3PbI_3$ layers were prepared by a

thermal-annealing induced interdiffusion of the two perovskite precursors (PbI$_2$, CH$_3$NH$_3$I): a method which had been recently developed by us to fabricate very efficient solar cells with high yield [8]. In brief, lead iodide (PbI$_2$) films were deposited by spin-coating on ITO/glass substrates first. A second layer consisting of methylammonium iodide (CH$_3$NH$_3$I, hereafter MAI) was then spin-coated on the top of the dried PbI$_2$ film, followed by thermal annealing at 105 °C for 60 min. Scanning electron microscopy (SEM) (**Figure S1**) shows that the inter-diffusion method enables the preparation of CH$_3$NH$_3$PbI$_3$ films on ITO that are continuous and uniform, which is particularly important to obtain leakage-free photodetectors. The absorption curve in **Figure 1b** shows that the CH$_3$NH$_3$PbI$_3$ films have a broad absorption spectrum ranging between 300 nm (UV) to 800 nm (NIR).

The photo- and dark-current densities (J)-voltage (V) curves of CH$_3$NH$_3$PbI$_3$ photodetectors (**Figure 1c**) show a transition from a diode-rectifying behavior in the dark, to photoconduction under illumination. Under illumination, both the forward and the reverse bias currents increased dramatically, with the reverse bias current increasing more sharply than the forward bias current. The rectifying effect completely disappeared, and an ohmic conduction behavior (symmetrical photocurrent with respect to y axis) was observed when exposing the device to white light irradiation (10 mW/cm^2). For comparison, J-V curve of a high performance solar cell (where exactly the same CH$_3$NH$_3$PbI$_3$ fabrication procedure was applied) with almost 100% external quantum efficiency under the same light intensity is also shown in **Figure 1c.** The reference photovoltaic (PV) device has a structure of ITO/PEDOT:PSS/MAPbI$_3$/[6,6]-phenyl-C61-butyric acid methyl ester (PCBM 20 nm)/C60 (20 nm)/2,9-dimethyl-4,7-diphenyl-1,10-phenanthroline (BCP, 8 nm)/aluminium (Al, 100 nm)[8]. Although photodetector exhibits a similar structure with that of the reference PV device, PCBM and C60 passivation layers were

intentionally omitted to leave surface trap states in photodetectors because fullerenes basically can passivate most of the charge traps. The photocurrent biased at -1 V is more than 100-fold larger for the $CH_3NH_3PbI_3$ photodetector device than for the photovoltaic device, highlighting the large gain provided by the perovskite photodetector. The device's peak responsivity (R), defined by the ratio of the photocurrent density at -1 V and the incident white light intensity, was calculated to be 56 A/W $\pm$ 2 A/W. The uncertainties through the manuscript represent a single standard deviation in the measurements on nominally identical devices.

Incident photon-to-current efficiency (IPCE) measurements can provide the device photoconductor gain directly by providing the number of charges flowing through an external circuit per incident photon. An IPCE value of 100 % corresponds to a photodetector gain value of 1. It should be noted that, in absence of a charge multiplication mechanism[2, 12], the IPCEs measured at 0 V bias are generally below 100% for photovoltaic devices, because all the charges that flow through the external circuit are photo-generated. In contrast, a photoconductor can have IPCEs above 100% because, in addition to the photo-generated charges, charges are also injected by the electrodes under an applied bias. Since the injected charges can be significantly more than the photo-generated charges, the resulting photovoltaic gain can be much larger than 1. IPCE measurements were performed at reverse biases between 0 V and -1 V at a 0.2 V steps. As shown in **Figure 1b**, the IPCE curves agree well with the profile derived from the absorption curve. The gain of the $CH_3NH_3PbI_3$ device increased as a function of the reverse bias from 0.3 at zero bias and exceeded 1 at -0.4 V. At -1 V, the gains reached 299 ± 6, 475 ± 6 and 405 ± 6 at 350 nm, 530 nm and 740 nm, respectively. The device's wavelength-dependent responsivity can be calculated from the wavelength dependent gain by:

$$R(\lambda) = \frac{Gain\,(\lambda)}{E_{hv}} \tag{1}$$

where E_{hv} is the energy of the incident photon (in eV). We obtain device responsivities of 84 A/W, 203 A/W and 242 A/W, at the three wavelengths respectively.

The large gain measured provides evidence that perovskite devices work as photoconductors under illumination. A photoconductive gain is obtained when a photon-generated transporting charge can travel through the circuit multiple times before recombination, because the charge recombination lifetime (τ_r) is larger than the charge transit time (τ_t), the drift time needed for charges to travel from one electrode to the opposite electrode under applied field, with the gain determined by τ_r/τ_t [13]. In contrast with a rectifying Schottky junction in a photodiode, a photoconductor requires a semiconductor-metal ohmic contact to supply sufficient circulating charge. In the dark there are large energy barriers for electron injection from MoO_3/Ag electrode to the OTP layer, and for hole injection from ITO to the OTP layer, which explains the rectification behavior in the dark. One of these two contacts must change from Schottky-junction to ohmic contact when the device is illuminated. To explain this behavior, we hypothesize that one type of trapped charges in the $CH_3NH_3PbI_3$ active layer induces band bending in the perovskite layer close to one of the electrodes, thus reducing the Schottky junction thickness, and allowing the injection of the opposite charges under reverse bias [4, 14]. Either the anode or the cathode interface could in principle undergo such transition when illuminated. To identify which contact turns to ohmic under illumination, single-carrier blocking layers were inserted at both interfaces between the OTP layer and the anode/cathode. It is expected that by inserting a thick charge transport buffer layer the transition from Schottky-junction to ohmic contact will be hindered, preventing charge tunneling from the electrode and eliminating the gain. Electron transport layers consisting of C_{60} or 2,9-

dimethyl-4,7-diphenyl-1,10-phenanthroline (BCP) were inserted between ITO and OTP, and an hole transport layer (TPD-Si$_2$) was inserted between OTP and MoO$_3$/Ag electrode. Almost no change in the maximum gain values was observed by increasing the thickness of BCP or C$_{60}$ from 20 nm to 60 nm (**Figure 1d**). On the contrary the maximum gain values were reduced dramatically by increasing the thickness of the TPD-Si$_2$ layer as shown in **Figure 1d**. This suggests that the ohmic contact is formed at the top interface between OTP and MoO$_3$/Ag electrode, and that hole-traps should be abundant on the top surface of the perovskite films (**Figure 1e**).

A large density of trap states in perovskite films was observed by a few experimental studies [9, 10], despite first-principles density-functional theory (DFT) calculations suggested that point defects in MAPbI$_3$ (MA = CH$_3$NH$_3$) do not generate trap states within the material band gap[11]. Previously we used thermal admittance spectroscopy (TAS) analysis to reveal trap densities as large as 10^{18} m^{-3} or 10^{19} m^{-3} in the pristine MAPbI$_3$ films[7]. This discrepancy may be reconciled if a large density of traps is confined at the perovskite film top surface while the trap density in the film bulk remain very small. This occurrence may be explained by the decomposition at the perovskite surface upon thermal annealing. Compared to the traditional inorganic semiconductors, the hybrid OTPs like MAPbI$_3$ are less thermally stable, which can be explained by the low dissociation energy of MAPbI$_3$.[15] The MAPbI$_3$ decomposition temperature is 300 °C,[16] but the decomposition at surfaces or grain boundaries may occur at much lower temperatures. Here we have applied the photothermal induced resonance (PTIR) technique to study the surface decomposition of perovskite films. PTIR is a novel technique combining the lateral resolution of atomic force microscopy (AFM) with the chemical specificity of IR spectroscopy thus enabling the acquisition of IR absorption spectra and maps with nanoscale resolution[17, 18, 19]. PTIR uses total internal reflection to illuminate the sample and an AFM tip in contact mode as a

near-field detector to transduce the thermal expansion induced by light absorption in the sample for gathering local chemical information (**Figure 2a**). Notably, for thin samples (< 1 μm)[18] the PTIR signal is proportional to the sample absorbed energy. For this study we built a custom enclosure, that allow recording PTIR data under nitrogen flow, and a temperature stage that allow annealing the sample in situ. A perovskite film was spun on an IR transparent prism, measured as prepared and after annealing at 140 °C, which is close to the device annealing temperature, for 10 min, 30 min and 60 min. Since the vibrational modes involving Pb occurs at much lower frequency than the PTIR spectral range[19], the spectra and images presented here essentially probe the MAI component of the perovskite material. The surface topography map and PTIR chemical map at 1468 cm^{-1} (corresponding to the CH_3 anti-symmetric stretching of the methylammonium ion) of the as-prepared MAPbI3 film are shown in **Figure 2c** and **2d** respectively and used as reference. After annealing for 10 min surface topography map (**Figure 2e**) show either minimal or no obvious change with respect to the as prepared film; however, PTIR chemical map (**Figure 2f**) shows that distinct striations appear. Representative PTIR spectra (**Figure 2b**) recorded from grains with striations, as a function of annealing time (0 min (as-prepared), 10 min, 30 min and 60 min) of the MAPbI3 film show an obvious suppression of of the CH_3 anti-symmetric stretching of the metyl ammonium ion at 1468 cm^{-1}. Since the PTIR intensity refers to the MAI content, and since the PTIR signal isproportional to the absorbed energy, this suggests a reduction of the MAI content in the MAPbI3 film upon annealing providing direct evidence of surface decomposition of MAPbI3. We attribute the striations in the PTIR image to the onset of MAI loss, which should leave a rich PbI2 film surface. Since Pb is not volatile we speculate that the surface decomposition leaves a large density of Pb^{2+} clusters on the film surface, which are the origin of the charge traps in the photodetector devices. For longer annealing the surface decomposition is more obvious, and leads

to an increase in surface roughness and heterogeneity in the PTIR images. An electron paramagnetic resonance study by *Shkrob et al.* [10] showed that Pb^{2+} clusters act indeed as hole traps which is also supported by our calculations (see below).

The first-principles calculations were performed within the framework of density functional theory [20]. Ion-electron interation was treated with the projector augment waves (PAW) approximation [21]. The optB88-vdW functional[22] was adopted for the exchange-correlation potential, which has been shown to provide the best agreement between the computed structural parameters and the experimental crystallographic parameters of $MAPbI_3$[23]. Surfaces cleaved along [001] direction with PbI_2- and MAI-termination were contructed where the bottom Pb atoms were passivated by H atoms. To simplify the calculation, we considered the simplest Pb cluster, i.e. a Pb dimer, which was added onto a $2{\times}2$ PbI_2-terminated surfaces to examine possible origin of the trap states, as shown in **Figure 3a**. The computed electronic band structures and density of states (DOS) of PbI_2-terminated surface with a Pb dimer (per supercell) are illustrated in **Figures 3b and 3c**, and show that the Pb^{2+} dimers cause both hole and electron traps. We note that the electron traps were not evident in our devices as well as in other solar cells devices, which is attributed to the passivation effect of the conducting polymer coating the perovskite surface or to electrons repulsion from the surface due to the applied electric field. The trap passivation of the TPD-Si$_2$ layer has been demonstrated in organic light-emitting diodes, because of its ability of terminating surface dangling bonds, eliminating adsorbed water and interacting with oxide electrode surfaces [24]. Nevertherless, our DFT calculation revealed an origin of the hole traps and its correlation with small-sized Pb clusters.

Having identified the nature of charge traps on the OTP surface, we can modulate the density of hole traps (i.e. the device gain) by varying the composition of the perovskite films. Here,

MAPbI$_3$ layers were optimized for the best device performance by evaluating the precursor ratio (PbI$_2$/MAI) during the film formation process. The maximum gain of the MAPbI$_3$ photodetectors was strongly affected by the PbI$_2$/MAI weight ratio (**Figure 4a),** and peaked at 600 mg/mL for PbI$_2$ with a fixed MAI concentration (43 mg/mL). **Table S1** provides the MAPbI$_3$ layer thickness obtained by varying the PbI$_2$ concentration from 400 mg/mL to 800 mg/mL and a fixed MAI concentration of 43 mg/mL. The maximum gain of the MAPbI$_3$ photodetectors were also influenced by the MAPbI$_3$ layer thickness, as shown in **Table S1**, and was the maximum for a MAPbI$_3$ thickness between 360 nm and 410 nm. In principle, a large thickness can result in smaller photo responses, but the challenge is the difficulty to separate the thickness change and composition change since both of them changes in our films. The concentrations that gave the best device performance here differs from that used to realize MAPbI$_3$ solar cells (400 mg/mL for PbI$_2$ and 45 mg/mL for MAI) [8] even if exactly the same fabrication procedure was applied. This suggests that a PbI$_2$ richer composition favors a larger density of hole traps on the top surface, reinforcing our findings (Pb^{2+} cations act as hole traps).

The temporal response of the photocurrent was evaluated by using a 532 nm laser with a light intensity of around 0.2 mW/cm^2 modulated with a chopper at 3,000 Hz (**Figure 4b)**. The device shows a short rise time of 10 µs $\pm$ 0.8 µs (from 10% to 90% of its peak value), and a biexponential photocurrent decay with time constant of 5.7 µs $\pm$ 1.0 µs and 41 µs $\pm$ 3.2 µs for the fast and slow component respectively. Both the rise time and decay time should be limited by the charge trapping/detrapping process because all other processes, such as charge generation and carrier drifting, should be much faster. The photocurrent multi-exponential decay indicates the existence of two recombination channels for the trapped holes, probably related to hole traps with different

trap depths. The gain (G) of the MAPbI$_3$ photodetector can also be calculated by the measured carrier recombination lifetime and transit time which is determined by

$$G = \frac{\tau_{lifetime}}{\tau_{transit\ time}} = \frac{\tau_{lifetime}}{d^2/\mu V} \tag{2}$$

where d is the device thickness, V is the applied bias and μ is the carrier mobility in the direction across the film. Here, the carrier recombination lifetime is 5.7 µs, V = 0.75 V, d = 390 nm, $\mu \approx$ 1.5·10^{-2} cm^2/V·s [8], leading to a calculated photoconductor gain of 43 ± 7.5 which is close to the measured gain by the IPCE method at the same bias.

A desirable characteristic for a photodetector is to have an identical responsivity over a wide range of light intensity, which is known as the linear dynamic range (LDR). The LDR was measured by recording the photocurrent of the CH$_3$NH$_3$PbI$_3$ photodetector under 532 nm laser illumination with light intensity from 6.9·10^{-9} mW/cm^2 to 3.6 mW/cm^2 (**Figure 4c**). The CH$_3$NH$_3$PbI$_3$ photodetector exhibited linear response with light intensity ranging from 6.9·10^{-9} mW/cm^2 to 0.23 mW/cm^2, corresponding to a LDR of 85 dB. Under stronger illumination, the device photocurrent deviated from the linear relationship with a lower output, which explains the discrepancy of the responsivities obtained with IPCE and photocurrent since they were measured with different light intensities.

Noise equivalent power (NEP) represents the weakest light intensity measurable by a photodetector or the light intensity threshold below which the photocurrent can no longer be distinguished from the noise current. The devices NEP was directly measured for the first time here by measuring the signal current together with noise current under various light intensities. A chopper modulated 532 nm laser (35 Hz) was used to illuminate the device, and the frequency dependent photocurrent signal, under the reverse bias of -0.7 V, was recorded by a FFT spectrum

analyzer. As shown in **Figure 4d**, in addition to the 1/f noise background, a peak at 35 Hz was observed with intensity decreasing as a function of the incident light intensity. The lowest detectable light intensity (at 35 Hz) was ≈ 6.2 pW/cm^2, or 0.37 pW for a device area (6 mm^2). The NEP can also be calculated by:

$$\text{NEP} = \frac{\overline{I_n^2}^{1/2}}{R}$$

(3)

where $\overline{i_n^2}^{1/2}$ is the total noise current and R is the responsivity. The NEP was calculated to be 0.18 pW, which is smaller but close to the measured NEP and is also close to the LDR measurement (0.4 pW). The excellent weak light detection capability of the perovskite photodetector benefits from the low noise enabled by the cross-linked TPD-Si$_2$ buffer layer, as well as the high gain due to the charge injection induced by the interfacial traps.

In addition to reducing the noise current, the cross-linked TPD-Si$_2$ electron blocking layer also improves the device stability by encapsulating the perovskite active layer. No discernable degradation of gain was observed after storing the as-prepared OTP photodetector in air at room temperature for more than three weeks (**Figure 4e**), indicating the cross-linked hydrophobic TPD-Si$_2$ layer effectively prevents the permeation of moisture to the perovskite layer. Photocurrent hysteresis provides a challenge for measuring efficiency accurately in perovskite photovoltaic devices[25]. For a photodetector, a reproducible photocurrent output is needed for determining the light intensity accurately. Here we measured the photocurrent at low light intensity which is of greater interest for practical applications. The photocurrent output of the OTP photodetector was recorded by increasing/decreasing the irradiation intensity repeatedly (**Figure 4f**). Clearly the

photodetectors showed excellent reproducibility in detecting weak light and no obvious hysteresis was discerned.

In summary, we reported a highly sensitive OTP based photodetector with a broadband response ranging from the UV to the NIR. The $CH_3NH_3PbI_3$ photodetectors showed a very high responsivity of 242 A/W at low bias (-1 V). The hole traps caused by large concentration of Pb^{2+} cations in the perovskite film top surface is critical for achieving high gain in these devices. The extremely low bias needed for the OTP photodetectors enables powering them with miniature button batteries and/or compact integration with existing low voltage circuits.

Reference

[1]	X. Gong, M. Tong, Y. Xia, W. Cai, J. S. Moon, Y. Cao, G. Yu, C.-L. Shieh, B. Nilsson, A. J. Heeger, *Science* **2009**, 325, 1665.

[2]	G. Konstantatos, E. H. Sargent, *Nat. Nano.* **2010**, 5, 391.

[3]   a) G. Konstantatos, I. Howard, A. Fischer, S. Hoogland, J. Clifford, E. Klem, L. Levina, E. H. Sargent, *Nature* **2006**, 442, 180; b) H.-Y. Chen, K. F. LoMichael, G. Yang, H. G. Monbouquette, Y. Yang, *Nat. Nano.* **2008**, 3, 543.

[4]   R. Dong, C. Bi, Q. Dong, F. Guo, Y. Yuan, Y. Fang, Z. Xiao, J. Huang, *Adv. Opt. Mater.* **2014**, 2, 549.

[5]   M. A. Green, A. Ho-Baillie, H. J. Snaith, *Nat. Photon.* **2014**, 8, 506.

[6]   a) A. Kojima, K. Teshima, Y. Shirai, T. Miyasaka, *J. Am. Chem. Soc.* **2009**, 131, 6050; b) J. Burschka, N. Pellet, S.-J. Moon, R. Humphry-Baker, P. Gao, M. K. Nazeeruddin, M. Gratzel, *Nature* **2013**, 499, 316; c) M. Liu, M. B. Johnston, H. J. Snaith, *Nature* **2013**, 501, 395; d) H. Zhou, Q. Chen, G. Li, S. Luo, T.-b. Song, H.-S. Duan, Z. Hong, J. You, Y. Liu, Y. Yang, *Science* **2014**, 345, 542.

[7]   Q. Wang, Y. Shao, Q. Dong, Z. Xiao, Y. Yuan, J. Huang, *Energ. Environ. Sci.* **2014**, 7, 2359.

[8]   Z. Xiao, C. Bi, Y. Shao, Q. Dong, Q. Wang, Y. Yuan, C. Wang, Y. Gao, J. Huang, *Energ. Environ. Sci.* **2014**, 7, 2619.

[9]   J. Kim, S.-H. Lee, J. H. Lee, K.-H. Hong, *J. Phys. Chem. Lett.* **2014**, 5, 1312.

[10]   I. A. Shkrob, T. W. Marin, *J. Phys. Chem. Lett.* **2014**, 5, 1066.

[11]   W.-J. Yin, T. Shi, Y. Yan, *Appl. Phys. Lett.* **2014**, 104, 063903.

[12]   K.-J. Baeg, M. Binda, D. Natali, M. Caironi, Y.-Y. Noh, *Adv. Mater.* **2013**, 25, 4267.

[13]   a) K. K. N. S. M. Sze, *Physics of Semiconductor Devices*, Wiley-Interscience, New Jersey **2007**; b) J. M. Liu, *Photonic Devices*, Cambridge University Press, New York **2005**.

[14]   F. Guo, B. Yang, Y. Yuan, Z. Xiao, Q. Dong, Y. Bi, J. Huang, *Nat. Nano.* **2012**, 7, 798.

[15]   a) A. Dualeh, N. Tétreault, T. Moehl, P. Gao, M. K. Nazeeruddin, M. Grätzel, *Adv. Func. Mater.* **2014**, 24, 3250; b) C. Bi, Y. Shao, Y. Yuan, Z. Xiao, C. Wang, Y. Gao, J. Huang, *J. Mater. Chem. A* **2014**, 2, 18508.

[16]   T. Baikie, Y. Fang, J. M. Kadro, M. Schreyer, F. Wei, S. G. Mhaisalkar, M. Graetzel, T. J. White, *J. Mater. Chem. A* **2013**, 1, 5628.

[17]   a) A. M. Katzenmeyer, J. Canivet, G. Holland, D. Farrusseng, A. Centrone, *Angew. Chem. Int. Edit.* **2014**, 53, 2852; b) A. Dazzi, R. Prazeres, F. Glotin, J. M. Ortega, *Opt. Lett.* **2005**, 30, 2388.

[18]   B. Lahiri, G. Holland, A. Centrone, *Small* **2013**, 9, 488.

[19]   A. M. Katzenmeyer, V. Aksyuk, A. Centrone, *Anal. Chem.* **2013**, 85, 1972.

[20]   G. Kresse, J. Furthmüller, *Phys. Rev. B* **1996**, 54, 11169.

[21]   P. E. Blöchl, *Phys. Rev. B* **1994**, 50, 17953.

[22]   a) M. Dion, H. Rydberg, E. Schröder, D. C. Langreth, B. I. Lundqvist, *Phys. Rev. Lett.* **2004**, 92, 246401; b) J. Klimeš, D. R. Bowler, A. Michaelides, *Phys. Rev. B* **2011**, 83, 195131.

[23]   E. Menéndez-Proupin, P. Palacios, P. Wahnón, J. C. Conesa, *Phys. Rev. B* **2014**, 90, 045207.

[24]   J. Cui, Q. Huang, J. C. G. Veinot, H. Yan, Q. Wang, G. R. Hutchison, A. G. Richter, G. Evmenenko, P. Dutta, T. J. Marks, *Langmuir* **2002**, 18, 9958;

[25]   H. J. Snaith, A. Abate, J. M. Ball, G. E. Eperon, T. Leijtens, N. K. Noel, S. D. Stranks, J. T.-W. Wang, K. Wojciechowski, W. Zhang, *J. Phys. Chem. Lett.* **2014**, 5, 1511.

(a)

Ag

TPD-Si$_2$

MoO$_3$

Perovskite

ITO

(b)

Gain

Absorption (%)

-1.0V
-0.8V
-0.6V
-0.4V
-0.2V
0V

Wavelength (nm)

(c)

Current Density (mA cm^{-2})

Photodetector
Photocurrent

Photovoltaic
Photocurrent

Photodetector
Dark Current

Voltage (V)

(d)

Maximum Gain

ITO/BCP(C60)/CH$_3$NH$_3$PbI$_3$/MoO$_3$/Ag

ITO/CH$_3$NH$_3$PbI$_3$/TPD-Si$_2$/MoO$_3$/Ag

Buffer Layer Thickness (nm)

(e)

-2.3 eV

TPD-Si$_2$

1

2

ITO (+)

MoO$_3$/Ag (-)

-5.5 eV

CH$_3$NH$_3$PbI$_3$

15
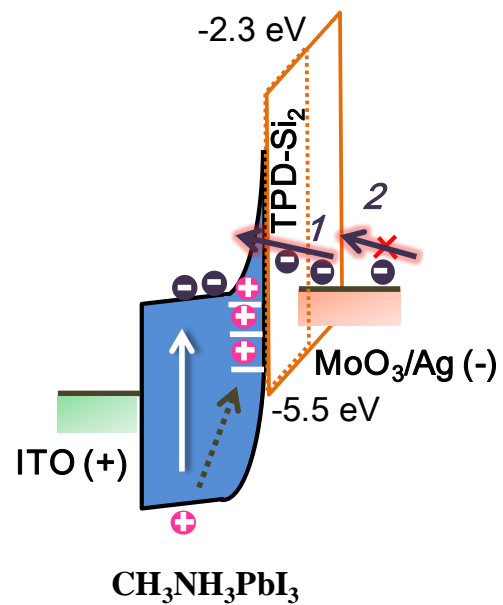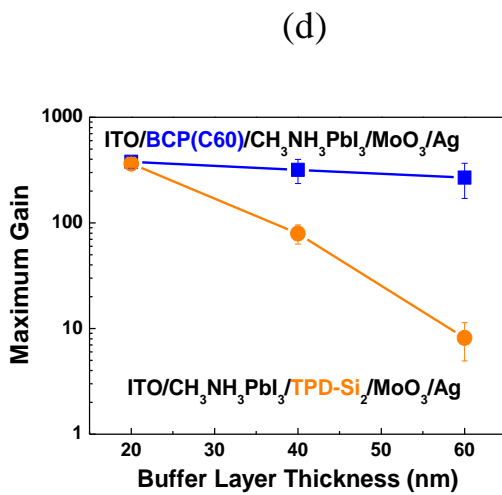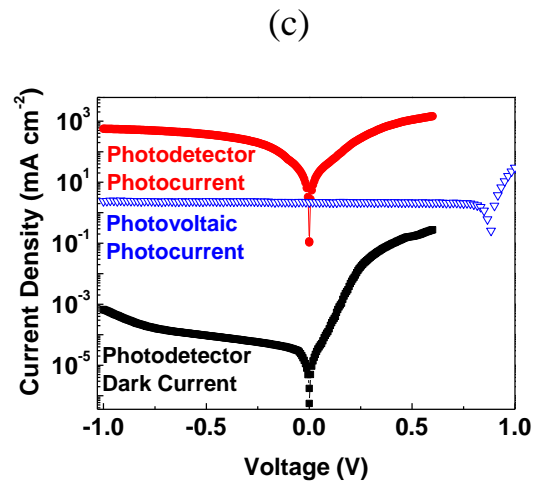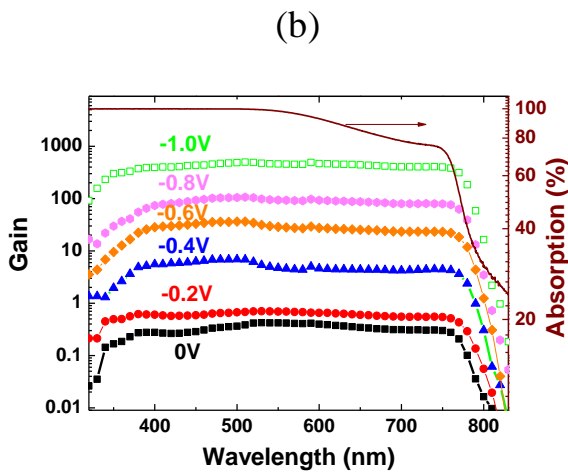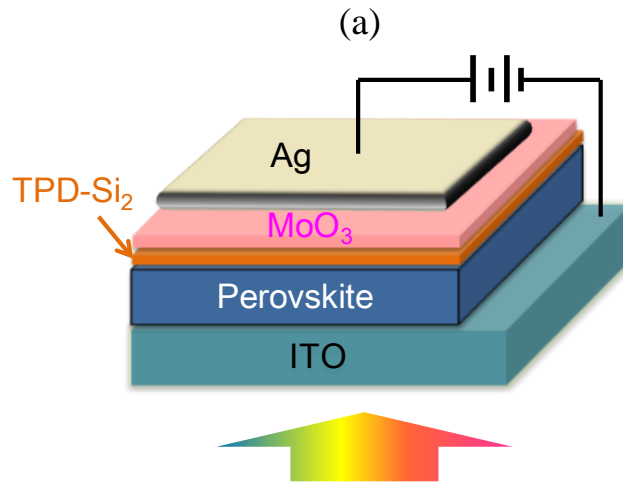
Figure 1. a) Device structure of the $CH_3NH_3PbI_3$ photodetector; b) Absorption spectrum (solid line) of the $CH_3NH_3PbI_3$ films and wavelength-dependednt gain (solid lines with symbols) of the $CH_3NH_3PbI_3$ devices under reverse biases between 0 V to -1 V; c) Photo- and dark-current density (J) - voltage (V) curves of the $CH_3NH_3PbI_3$ device. The reference PV device has a structure of ITO/PEDOT:PSS/MAPbI_3/PCBM/C60/BCP/Al; d) The dependence of maximum gain values of the $CH_3NH_3PbI_3$ photodetectors on the thickness of single carrier blocking layers; e) Energy diagram of the $CH_3NH_3PbI_3$ photodetector at reverse bias under illumination.
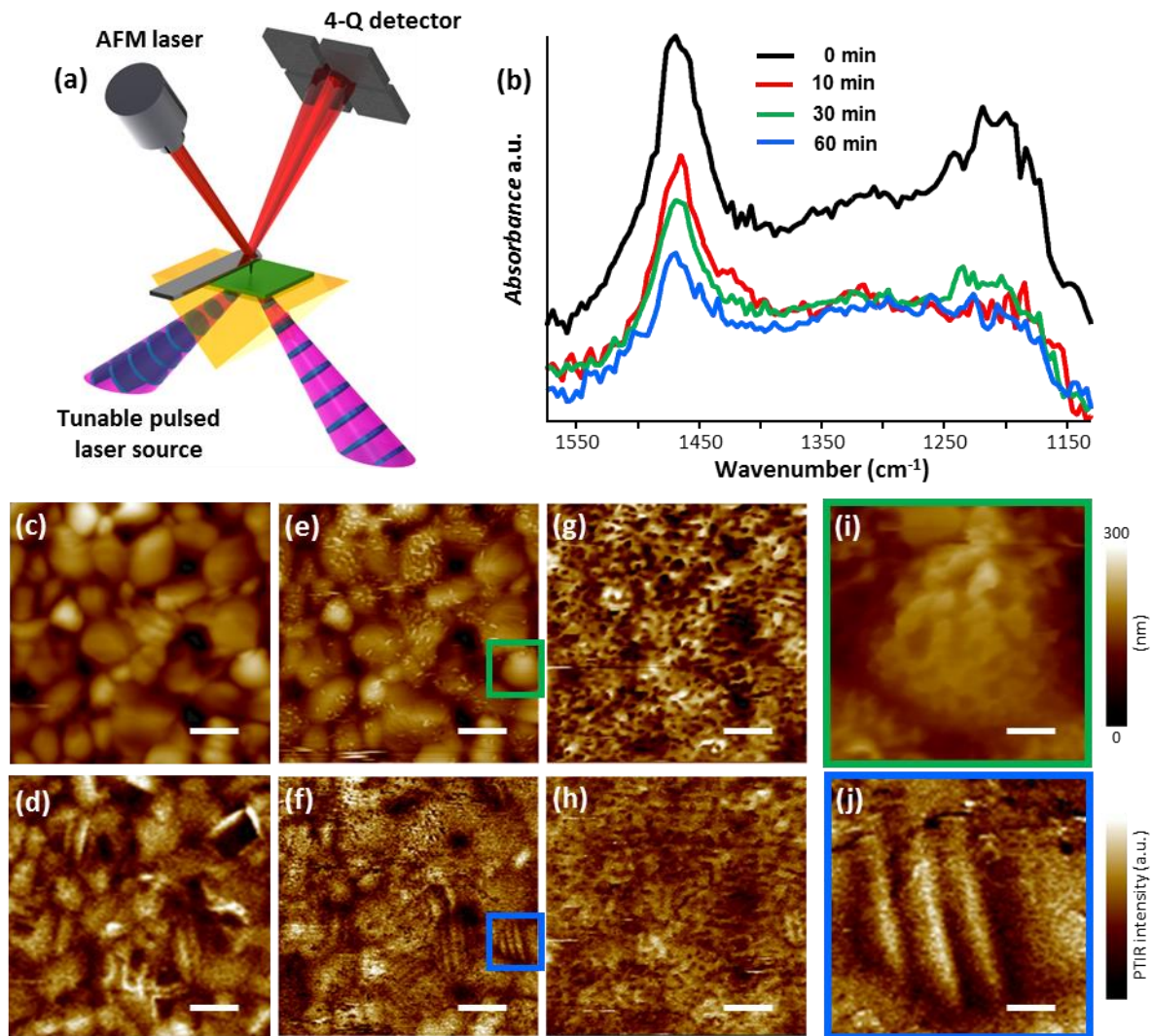
Figure 2. a) Schematic of the PTIR experimental setup; b) PTIR spectra as a function of annealing time. c-h) Height and PTIR images of the same sample area before annealing (c and d), after annealing for 10 min (e and f) or 60 minutes (g and h). All scale bars in panels c-h are 1 μm. i,j) High resolution height and PTIR images of the sample area marked by a color-coded boxes in figure 3 e,f obtained after 30 min of annealing. Scale bars in panels i, j are 200 nm. All PTIR images were recorded at 1468 cm^{-1} corresponding to the CH$_3$ antisymmetric stretching of the methylammonium ion.
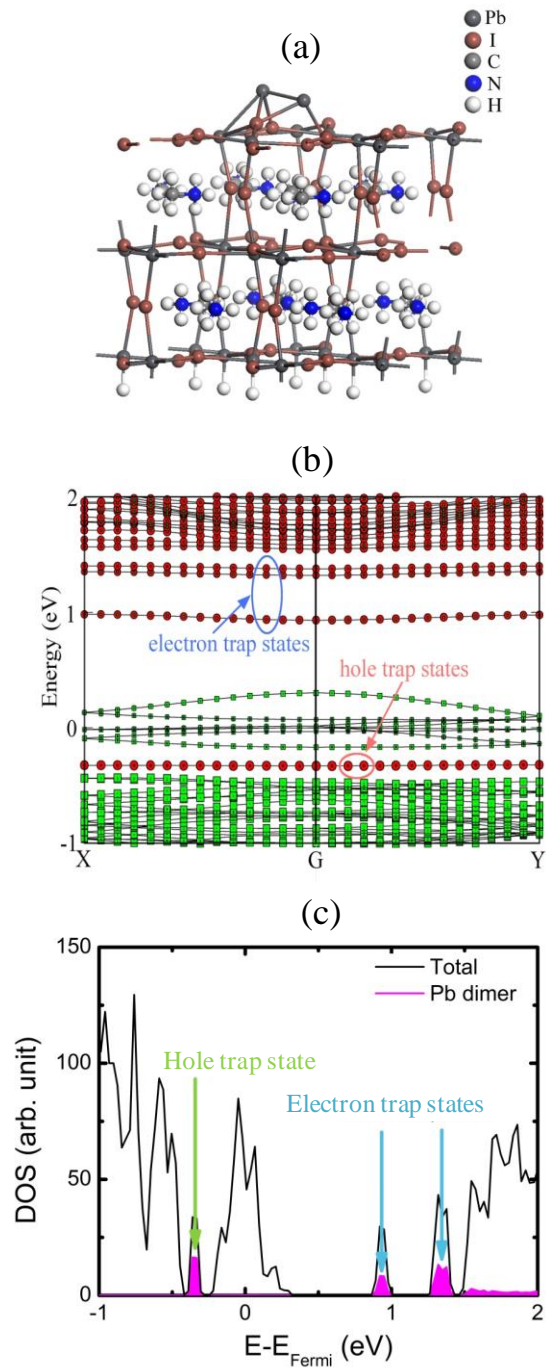
Figure 3. a) Schematic view; b) the computed electronic band structures, where the red and green spheres denote the contribution from Pb and I atoms, respectively; c) the computed density of states curves, where the partial density of states (pDOS) from the Pb dimer is highlighted in pink.

(a)

(b)

$\tau_1 = 5.7\ \mu s$

$\tau_2 = 41\ \mu s$

(c)

(d)

Light Intensity (pW cm^{-2})
- 6,200
- 2,000
- 620
- 200
- 62
- 20
- 6.2

(e)

(f)

- 1st scan
- 2nd scan
- 3rd scan
- (Reported LDR)

1 st

2 nd

3 rd
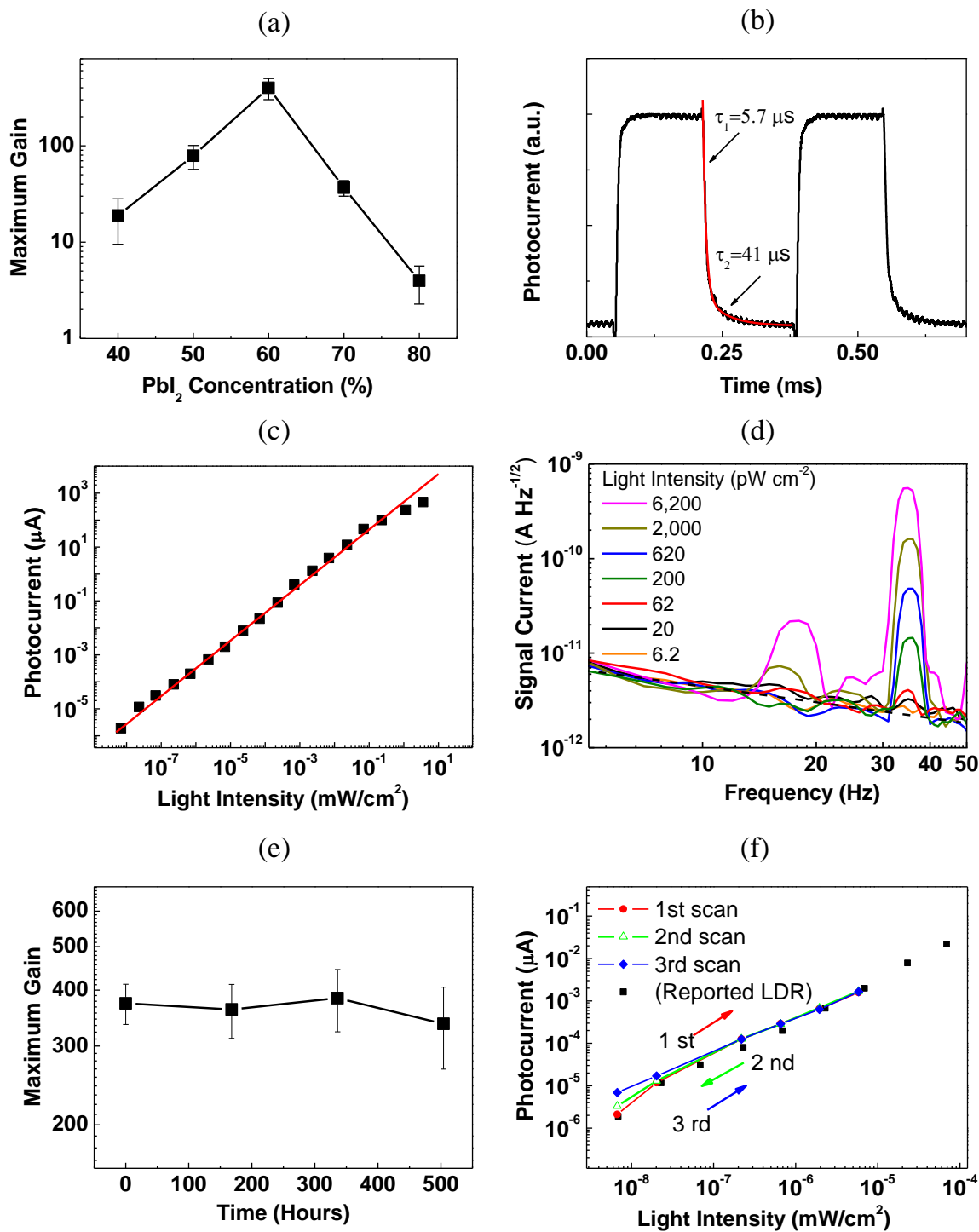
Figure 4. a) Maximum gain of the CH$_3$NH$_3$PbI$_3$ photodetectors as a function of the PbI$_2$/MAI relative mass fraction; b) Transient photocurrent of the CH$_3$NH$_3$PbI$_3$ photodetector; c) Dynamic response of the photodetector; d) The noise current spectrum of the photodetector measured with

various light intensities (the dashed line is the 1/f noise background); e) The gain of the OTP

photodetector measured in air at room temperature over three weeks; f) the weak light detection

of the CH₃NH₃PbI₃ photodetector after three circles of light intensity sweeping.

The table of contents

High Gain and Low-Driving-Voltage Photodetectors Enabled by Organolead Triiodide Perovskites

Rui Dong, Yanjun Fang, Jungseok Chae, Jun Dai, Zhengguo Xiao, Qingfeng Dong, Yongbo Yuan, Andrea Centrone, Xiao Cheng Zeng and Jinsong Huang[*]

Keywords: organolead triiodide perovskite, gain, photodetector, solution process, low bias
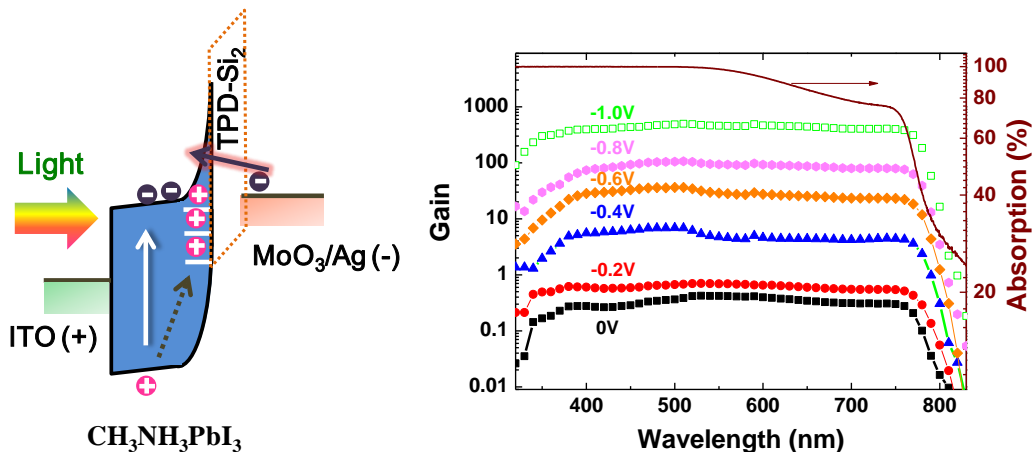
Solution-processed organometal trihalide perovskites photodetectors show a high photoconductive gain of above 400 from the UV to the NIR under a very low bias of -1 V. The hole traps caused by large concentration of Pb^{2+} cations in the perovskite film top surface is critical for achieving high gain in these devices via the trapped-hole induced electron injection mechanism.

High Gain and Low-Driving-Voltage Photodetectors Enabled by Organolead Triiodide Perovskites

Rui Dong[1], Yanjun Fang[1], Jungseok Chae[2,3], Jun Dai,[4] Zhengguo Xiao[1], Qingfeng

Dong[1],Yongbo Yuan[1], Andrea Centrone[2], Xiaocheng Zeng[4]and Jinsong Huang[1*]

[1]Department of Mechanical and Materials Engineering, University of Nebraska-Lincoln,

Lincoln, Nebraska 68588, USA.

[2]Center for Nanoscale Science and Technology, National Institute of Standards and Technology

100 Bureau Drive, Gaithersburg, MD 20899, USA.

[3]Maryland Nanocenter, University of Maryland, College Park, MD 20742 USA.

[4]Department of Chemistry, University of Nebraska-Lincoln, Lincoln, Nebraska 68588, USA.

*E-mail: jhuang2@unl.edu

Device fabrication and characterization: The MAPbI3 layers were prepared by an interdiffusion method. MAI was dissolved in 2-propanol to obtain a concentration of 43 mg/mL. PbI2 were dissolved in dimethylformamide with weight concentration ranging from 400 mg/mL to 800 mg/mL). The PbI2 solution was spun on ITO substrate at 100 Hz and dried at 70 °C. The MAI solution was spun on top of dried PbI2 film at 100 Hz and the layered films were dried at 100 °C for 1 h. TPD-Si2 (20 mg/mL) was dissolved in 1,2-dichlorobenzene (DCB) and spin coated on CH3NH3PbI3 active layers. The resulting films were then annealed at 100 ℃ for 1 hour in air to crosslink TPD-Si2. The combination of 12 nm MoO3 and 100 nm Ag was thermally evaporated on the photoactive layer as the cathode. The device active area is around 6 mm^2 controlled by a metal shadow mask.

The uncertainties through the manuscript represent a single standard deviation in the measurements on nominally identical devices (20 to 50 devices were measured for each condition). The steady-state photocurrent curves were measured under 10% of the simulated AM (air mass) 1.5 G (global) irradiation (10 mW/cm^2) using a Xenon-lamp-based solar simulator. The linear dynamic range was characterized by measuring the device photocurrent under -0.70 V at 35 Hz with 532 nm laser illumination of various laser intensities which were attenuated by neutral density filters and calibrated by a Si photodiode. The temporal response was measured by illuminating the device with a chopper-modulated 532 nm laser (3,000 Hz). The light turn-on time on the device was calculated to be 4 μs. The device was biased at -0.75 V and the transient photocurrent signal was recorded using a digital oscilloscope.

PTIR characterization: PTIR experiments were carried out using a commercial PTIR setup that consists of an AFM microscope operating in contact mode and a tunable pulsed laser source consisting of an optical parametric oscillator based on a noncritically phase-matched ZnGeP2 crystal. The laser emits pulses 10 ns long at 1 kHz repetition rate that are tunable from 4000 cm^{-1} to ≈ 1025 cm^{-1} (from 2.5 μm to 9.76 μm). The low repetition rate of the laser (1 kHz) assures that a new pulse will excite a sample and cantilever after they have returned to equilibrium. The typical laser spot size is ≈ 30 μm at the sample. PTIR experiments were obtained by flowing nitrogen gas (0.12 dm^3/s) in custom enclosure built around the sample.

The CH3NH3PbI3 film composition and thickness

The CH3NH3PbI3 layers in the perovskite photodetector were prepared by the interdiffusion method. Two steps of spin-coating, first PbI2 and then methylammonium iodide, were involved in the CH3NH3PbI3 film preparation procedure which is very convenient for controlling the composition of the peroskite films and the density of hole traps. In this study, CH3NH3PbI3 layers were optimized for the best device performance by varying the precursor concentration during the film preparation process. **Table S1** provides the CH3NH3PbI3 layer thickness obtained by varying the PbI2 concentration from 400 mg/mL to 800 mg/mL and a fixed CH3NH3I (MAI) concentration of 43 mg/mL.

CH₃NH₃I / PbI₂	43 mg/mL
400 mg/mL	260 nm to 280 nm
500 mg/mL	300 nm to 330 nm
600 mg/mL	360 nm to 410 nm
700 mg/mL	530 nm to 590 nm
800 mg/mL	610 nm to 670 nm

Table S1: The dependence of $CH_3NH_3PbI_3$ layer thickness on the varied PbI_2 and CH_3NH_3I weight concentration.

Scanning electron microscope (SEM) characterization of $CH_3NH_3PbI_3$ films

Figure S1 shows that the as-prepared $CH_3NH_3PbI_3$ films on the ITO substrate prepared with by the inter-diffusion method are continuous and uniform.
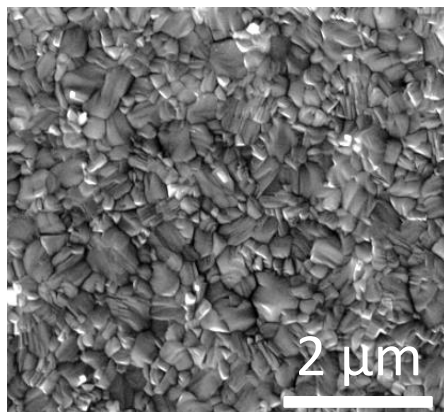

Figure S1 SEM image of the $CH_3NH_3PbI_3$ layer prepared with the inter-diffusion process.